

Fission fragment mass yields of Th to Rf even-even nuclei *

Krzysztof Pomorski^{1†}, José M. Blanco¹, Pavel V. Kostyukov¹, Artur Dobrowolski¹,
Bożena Nerlo-Pomorska¹, Michał Warda¹, Zhigang Xiao^{2‡}, Yongjing Chen³, Lile Liu³,
Jun-Long Tian⁴, Xinyue Diao², Qianghua Wu²

¹ Institute of Physics, Maria Curie Skłodowska University, 20-031 Lublin, Poland

² Department of Physics, Tsinghua University, Beijing 100084, China

³ China Institute of Atomic Energy, Beijing 102413, China

⁴ School of Physics and Electrical Engineering, Anyang Normal University, Anyang 455000, China

January 12, 2021

Abstract:

Fission properties of the actinide nuclei are deduced from theoretical analysis. We investigate potential energy surfaces and fission barriers and predict the fission fragment mass-yields of actinide isotopes. The results are compared with experimental data where available. The calculations were performed in the macroscopic-microscopic approximation with the Lublin-Strasbourg Drop (LSD) for the macroscopic part and the microscopic energy corrections were evaluated in the Yukawa-folded potential. The Fourier nuclear shape parametrization is used to describe the nuclear shape, including the non-axial degree of freedom. The fission fragment mass-yields of considered nuclei are evaluated within a 3D collective model using the Born-Oppenheimer approximation.

Keywords: nuclear fission, mac-mic model, fission barrier heights, fragment mass-yields

PACS: 21.10.Dr, 25.70.Ji, 25.85.-w, 25.85.Ec

*Supported by the Polish National Science Center (Grant No. 2018/30/Q/ST2/00185) and by the National Natural Science Foundation of China (Grant No. 11961131010 and 11790325).

[†]Email Krzysztof.Pomorski@umcs.pl

[‡]Email: xiaozg@mail.tsinghua.edu.cn

1 Introduction

Good reproduction of fission barrier heights and fission fragments mass-yields is a test of the theoretical models describing the nuclear fission process. An interesting review of the existing fission models can be found in Refs. [1, 2, 3]. Extended calculations of the fission barrier heights can be found in Refs. [4, 5]. Readers who are interested in the theory of nuclear fission can find more details in the textbook [6].

In the present paper, the fission fragment mass yields (FMY) are obtained by an approximate solution of the eigenproblem of a three-dimensional collective Hamiltonian, of which the coordinates correspond to the fission, neck, and mass-asymmetry modes. Here presented model is described in details in Refs. [7, 8, 9]. The potential energy surfaces (PES) of fissioning nuclei obtained by the macroscopic-microscopic (mac-mic) method in which the Lublin-Strasbourg Drop (LSD) model [10] has been used for the macroscopic part of the energy, while the microscopic shell and pairing corrections are evaluated using single-particle levels of the Yukawa-folded (YF) mean-field potential [11, 12]. The Fourier parametrization is used to describe shapes of fissioning nuclei [13, 14]. It is shown in Ref. [15] that this parametrization describes very well the shapes of the nuclei even close to the scission configuration.

The paper is organized in the following way. In Section 2, we present first the details of the shape parametrization and the theoretical model. Then we show the collective potential energy surface evaluated within the mac-mic model for the selected isotopes and our estimates of the fission barrier heights. The calculated FMY are compared with the existing experimental data in Section 3. The estimates of FMY for Th isotopes and their dependence on two adjustable parameters are further discussed in details in Section 4. Conclusions and perspectives of further investigations are presented in Section 5.

2 Model of the fission dynamics

The evolution of a nucleus from the equilibrium state towards fission is described here by a simple dynamical approach based on the PES. We assume that at large deformations, the shape of the nucleus should depend on three collective degrees of freedom describing its elongation, left-right asymmetry, and the neck-size. At smaller deformations, up to the second saddle, the non-axial shapes are also considered. In the following subsection, we present shortly a Fourier type parametrization of the nuclear shape which is used in the paper.

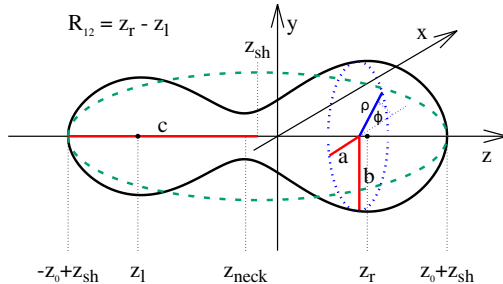


Fig. 1: Shape of a very elongated fissioning nucleus.

2.1 Fourier nuclear shape parametrization

A typical shape of the nucleus on the way from the saddle to the scission configuration is shown in Fig. 1, where $\rho(z)$, the distance from the z -axis to the surface of the nucleus as a function of z , is plotted. Here by the nuclear surface is treated the surface of the nuclear liquid drop, or the half-density surface when the microscopic density distribution is considered.

The function $\rho(z)$ corresponding to the nuclear surface can be expanded in the Fourier series in the following way [13]:

$$\rho_s^2(z) = R_0^2 \sum_{n=1}^{\infty} \left[a_{2n} \cos \left(\frac{(2n-1)\pi}{2} \frac{z-z_{sh}}{z_0} \right) + a_{2n+1} \sin \left(\frac{2n\pi}{2} \frac{z-z_{sh}}{z_0} \right) \right]. \quad (1)$$

Here z_0 is the half-length of the total elongation of the nucleus and z_{sh} locates the center of mass of the nucleus at the origin of the coordinate system. The expansion parameters a_i can serve as parameters describing the shape of nucleus. The length parameter $c = z_0/R_0$ is fixed by the volume conservation condition, where R_0 is the radius of spherical nucleus having the same volume as the deformed one.

Contrary to frequently used spherical harmonics expansion (conf. e.g., Refs. [4, 5]), the Fourier series converges much earlier for the realistic shape of nuclei [13, 14] and only a few first terms are sufficient in practical use. Although one can work directly with these Fourier expansion coefficients treating them as free deformation parameters, it is more suitable to use their combinations $\{q_n\}$,

called *optimal coordinates* [14], as following

$$\begin{cases} q_2 = a_2^{(0)}/a_2 - a_2/a_2^{(0)} \\ q_3 = a_3 \\ q_4 = a_4 + \sqrt{(q_2/9)^2 + (a_4^{(0)})^2} \\ q_5 = a_5 - (q_2 - 2)a_3/10 \\ q_6 = a_6 - \sqrt{(q_2/100)^2 + (a_6^{(0)})^2} \end{cases} \quad (2)$$

The functions $q_n(\{a_i\})$ were chosen in such a way that the liquid-drop energy as a function of the elongation q_2 becomes minimal along a trajectory that defines the liquid-drop path to fission. The $a_{2n}^{(0)}$ in Eq. (2) are the expansion coefficients of a spherical shape given by $a_{2n}^{(0)} = (-1)^{n-1} \frac{32}{\pi^3 (2n-1)^3}$. The above relations proposed in Ref. [14] transform the original deformation parameters a_i to the more natural parameters q_i , which ensure that only minor variations of the liquid-drop fission paths occur around $q_4 = 0$. In addition, more and more elongated prolate shapes correspond to decreasing values of a_2 , while oblate ones are described by $a_2 > 1$, which contradicts the traditional definition of the elongation parameter. The parametrization (2) is rapidly convergent. It was shown in Ref. [15] that the effect of q_5 and q_6 on the macroscopic potential energy of nuclei is negligible for small elongations of nuclei up to the saddle points and contributes within 0.5 MeV around the scission configurations.

Non-axial shapes can easily be obtained assuming that, for a given value of the z -coordinate, the surface cross-section (blue dashed oval in Fig. 1) has the form of an ellipse with half-axes $a(z)$ and $b(z)$ [14]:

$$\rho_s^2(z, \varphi) = \rho_s^2(z) \frac{1 - \eta^2}{1 + \eta^2 + 2\eta \cos(2\varphi)} \quad \text{with} \quad \eta = \frac{b - a}{a + b}, \quad (3)$$

where the parameter η describes the non-axial deformation of the nuclear shapes. The volume conservation condition requires that $\rho_s^2(z) = a(z)b(z)$.

2.2 Potential energy surfaces

The nuclear potential energies of actinide nuclei are evaluated in the following equidistant grid-points in the 4D collective space built on the q_2 , q_3 , q_4 , and η deformation parameters:

$$\begin{aligned} q_2 &= -0.60 \text{ (0.05) } 2.35, \\ q_3 &= 0.00 \text{ (0.03) } 0.21, \\ q_4 &= -0.21 \text{ (0.03) } 0.21, \\ \eta &= 0.00 \text{ (0.03) } 0.21. \end{aligned} \quad (4)$$

Here, the numbers in the parentheses are the step size, while the numbers on the left (right) side are the lower

(upper) boundaries of the grid, respectively. The energy of a nucleus is obtained in the mac-mic model, where the smooth energy part is given by the LSD model [10], and the microscopic effects have been evaluated using the YF single-particle potential [11, 12]. The Strutinsky shell-correction method [16, 17, 18] with a 6th order correctional polynomial and a smoothing width $\gamma_S = 1.2\hbar\omega_0$ is used to determine the shell energy correction, where $\hbar\omega_0 = 41/A^{1/3}$ MeV is the distance between the spherical harmonic-oscillator major shells. The BCS theory [19] with the approximate GCM+GOA particle number projection method [20] is used for the pairing correlations. An universal pairing strengths written as $G\mathcal{N}^{2/3} = 0.28\hbar\omega_0$, with $\mathcal{N} = Z, N$ for protons or neutrons, was adjusted in Ref. [21] to the experimentally measured mass differences of nuclei from different mass regions. It was assumed in Ref. [21] that the ‘‘pairing window’’ contains $2\sqrt{15\mathcal{N}}$ single-particle energy levels closest to the Fermi level. All the above parameters were fixed in the past, and none of them was specially fitted to the properties of actinide nuclei.

A typical PES for actinides is shown in Fig. 2, where two cross-sections (q_2, η) and (q_2, q_3) of the 4D potential energy surface of ^{240}Pu are shown. As one can see,

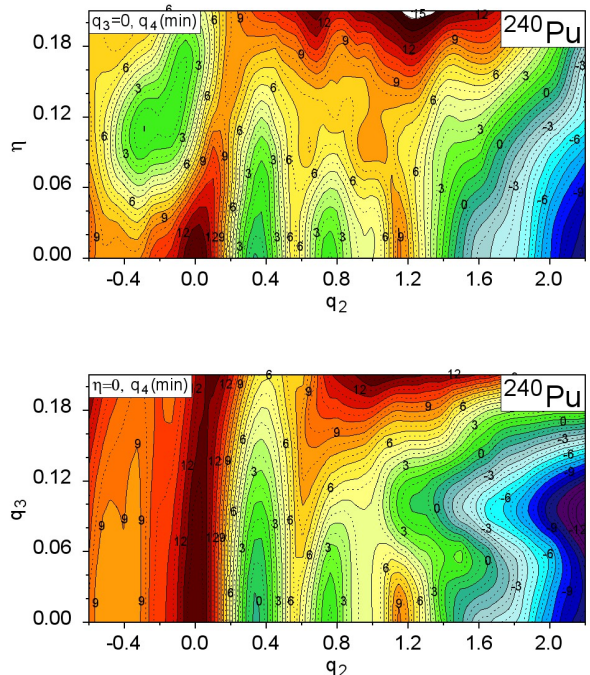


Fig. 2: Potential energy surface of ^{240}Pu minimized with respect to q_4 at the (q_2, η) (top map) and (q_2, q_3) (bottom) planes.

the inclusion of the non-axial deformation is important up to elongations corresponding to the second saddle

($q_2 \leq 1.2$). Apart of some neutron deficient actinide nuclei which have $q_3 \neq 0$ in the ground-state, the left-right asymmetry begins to play an important role at large elongations of nuclei, from the second saddle ($q_2 \approx 1$) up to the scission configuration ($q_2 \gtrsim 2$).

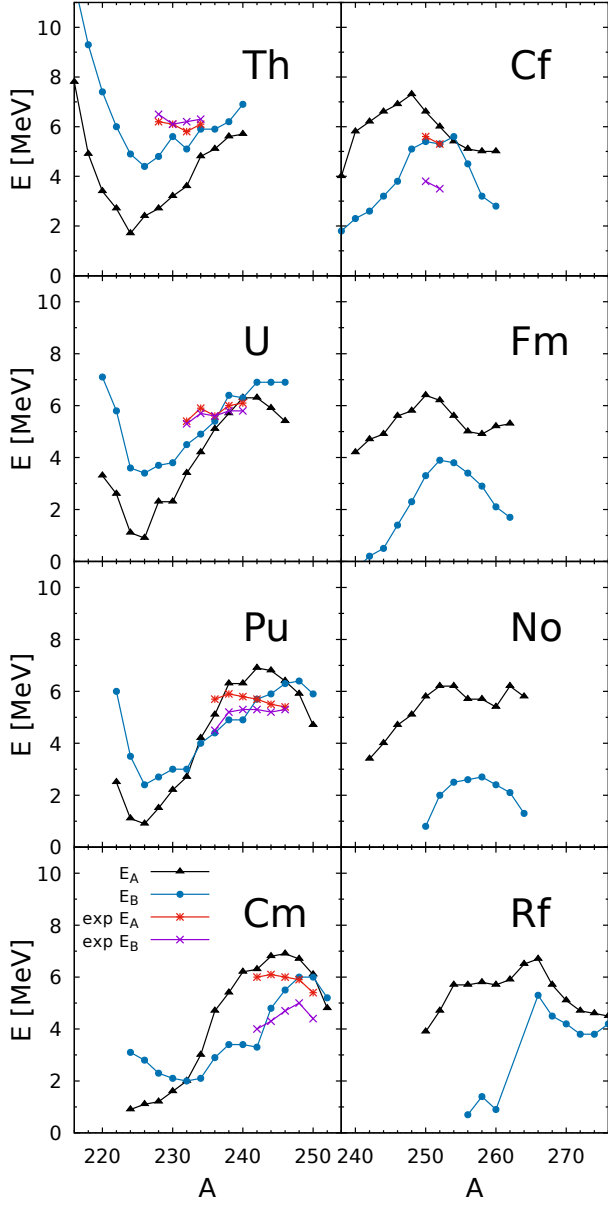


Fig. 3: Fission barrier heights of even-even actinide nuclei in our 4D mac-mic model.

The first (E_A) and the second (E_B) fission barrier heights obtained in our model for nuclei from Th to Rf are compared in Fig. 3 with the experimental data taken from Ref. [22, 3]. The agreement of our estimates with the data is rather satisfactory, and is comparable within an accuracy obtained in other theoretical models. The

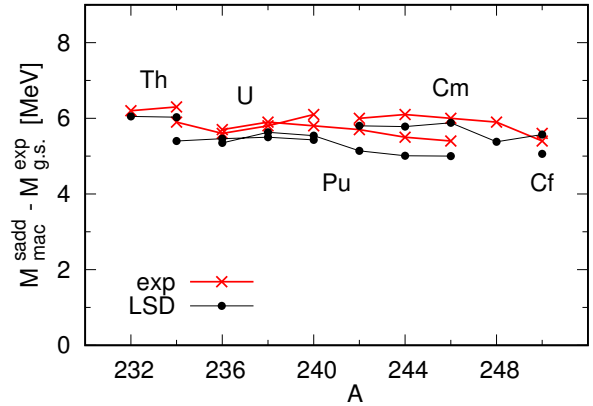


Fig. 4: Fission barrier heights of even-even actinide nuclei evaluated using the topographical theorem and the LSD model compared with the experimental barrier heights as a function of mass number A [24].

largest deviation between our estimates and the experimental values are observed in thorium isotopes, where they are underestimated. The main origin of these discrepancies is mostly from the inaccuracy of determining the ground-state masses in our model. To prove it, we have estimated the fission barrier heights using the so called topographical theorem of Myers and Świątecki [23], where the barrier height (the largest one) is defined as

$$E_{\text{barr}} = M_{\text{mac}}^{\text{sadd}} - M_{\text{g.s.}}^{\text{exp}}, \quad (5)$$

where $M_{\text{mac}}^{\text{sadd}}$ is the first barrier saddle point mass evaluated in the macroscopic model (i.e., without microscopic energy correction) and $M_{\text{g.s.}}^{\text{exp}}$ is the experimental ground-state mass of the nucleus.

Using the LSD model [10] to evaluate the macroscopic (read LD) mass one obtains the ‘Świątecki’ estimates of barrier heights, which deviate from the experimental data only by 310 keV on the average, as shown in Fig. 4. It means that additional work to improve the estimates of the ground-state masses has to be done. In particular, to make a better fit of the pairing strength. Our ‘universal’ pairing force [21], used in the present work, reproduces on average the pairing gaps of nuclei from different mass regions, but it might be that it does not reproduce perfectly the pairing properties in actinides.

2.3 Simple collective model for fission

The present research is a continuation and extension of our previous works [7, 8, 9], where more detailed description of the collective fission model was given. The fundamental idea of this approach is the use of the Born-Oppenheimer approximation (BOA) to separate the relatively slow motion towards fission, mainly in q_2

direction, from the fast vibrations in the “perpendicular” q_3 and q_4 collective coordinates. The BOA allows us to treat these both types of motion as decoupled, what leads, in consequence, to the wave function in form of the following product:

$$\Psi_{nE}(q_2, q_3, q_4) = u_{nE}(q_2) \phi_n(q_3, q_4; q_2) . \quad (6)$$

The function $u_{nE}(q_2)$ is the eigenfunction corresponding to the motion towards fission, while the $\phi_n(q_3, q_4; q_2)$ simulates the n -phonon “fast” collective vibrations in the “perpendicular” to the fission mode $\{q_3, q_4\}$ plane.

To determine the $u_{nE}(q_2)$ function for a single q_2 mode one can use the WKB approximation as it has been done in Ref. [7]. To obtain the function $\phi_n(q_3, q_4; q_2)$, one has to solve numerically for each value of q_2 the eigenproblem of the underlying Hamiltonian in the perpendicular $\{q_3, q_4\}$ space. However, for the low energy fission, it is sufficient to take only the lowest wave function in the perpendicular mode and evaluate the density of probability $W(q_3, q_4; q_2)$ of finding the system for a given elongation q_2 within the area of $(q_3 \pm dq_3, q_4 \pm dq_4)$ as

$$W(q_3, q_4; q_2) = |\Psi(q_2, q_3, q_4)|^2 = |\phi_0(q_3, q_4; q_2)|^2 . \quad (7)$$

Further simplification we have made is to approximate the modulus square of the total wave function in Eq. (7) by the Wigner function in the following form

$$W(q_3, q_4; q_2) \propto \exp \frac{V(q_3, q_4; q_2) - V_{\min}(q_2)}{T^*} , \quad (8)$$

where $V_{\min}(q_2)$ is the minimum of the potential for a given elongation q_2 and T^* is a generalized temperature [25] which takes into account both thermal excitation of fissioning nucleus and the collective zero-point energy E_0

$$T^* = E_0 / \tanh(E_0/T) . \quad (9)$$

The temperature (T) of nucleus with mass-number A is evaluated from its thermal excitation energy (E^*) using the phenomenological relation $E^* = aT^2$, with $a = A/(10 \text{ MeV})$. The generalized temperature T^* is approximately equal to the zero-point energy when T is small while for sufficiently high temperatures ($T \gg E_0$) it approaches to T . In the following E_0 is treated as one of two adjustable parameters of our model. Of course, one expects E_0 of the order of 1 to 2 MeV as implied by the energy level positions of typical collective vibrational states.

To obtain the FMY for a given elongation q_2 one has to integrate the probabilities (8) over the full range of the neck parameter q_4

$$w(q_3; q_2) = \int W(q_3, q_4; q_2) dq_4 . \quad (10)$$

It is rather obvious that the fission probability may strongly depend on the neck radius R_{neck} . Following

Ref. [7] one assumes the neck rupture probability P to be equal to

$$P(q_2, q_3, q_4) = \frac{k_0}{k} P_{\text{neck}}(R_{\text{neck}}) , \quad (11)$$

where P_{neck} is a geometrical factor indicating the neck breaking probability proportional to the neck thickness, while k_0/k describes the fact that the larger collective velocity towards fission, $v(q_2) = \dot{q}_2$, implies that the neck rupture between two neighboring q_2 configurations is getting less probable. The constant parameter k_0 plays the role of scaling parameter which is finally eliminated in the calculation of the resulting FMY. The expression for the geometrical probability factor $P_{\text{neck}}(R_{\text{neck}})$ is chosen here in a form of Gauss function [8]:

$$P_{\text{neck}}(R_{\text{neck}}) = \exp[-\log(2)(R_{\text{neck}}/d)^2] , \quad (12)$$

where d , our second adjustable parameter, is the “half-width” of the neck-breaking probability. The momentum k in Eq. (11) simulates the dynamics of the fission process, which, as usual, depends both on the local collective kinetic energy (E_{kin}) and the inertia (M) towards the fission mode

$$\frac{\hbar^2 k^2}{2\bar{M}(q_2)} = E_{\text{kin}} = E - E^* - V(q_2) , \quad (13)$$

with $\bar{M}(q_2)$ standing for the (averaged over q_3 and q_4 degrees of freedom) inertia parameter at a given elongation q_2 , and $V(q_2)$ is the potential corresponding to the bottom of the fission valley. In the further calculations we assume that the part of the total energy converted into heat E^* is negligibly small due to rather small friction forces in the low energy fission. A good approximation of the inertia $\bar{M}(q_2)$, proposed in Ref. [26], is to use the irrotational flow mass parameter B_{irr} , which is derived initially as a function of the distance between fragments R_{12} and the reduced mass μ of both fragments

$$\bar{M}(q_2) = \mu[1 + 11.5 (B_{\text{irr}}/\mu - 1)] \left(\frac{\partial R_{12}}{\partial q_2} \right)^2 . \quad (14)$$

In order to make use of the neck rupture probability $P(q_3, q_4; q_2)$ of Eq. (11), one has to rewrite the integral over q_4 in probability distribution (10) in the following form:

$$w(q_3; q_2) = \int W(q_3, q_4; q_2) P(q_2, q_3, q_4) dq_4 , \quad (15)$$

in which the neck rupture probability is now taken into account. The above approximation describes a very important fact that, for a fixed q_3 value, the fission may occur within a certain range of q_2 deformations with different probabilities. Therefore, to obtain the true fission

probability distribution $w'(q_3; q_2)$ at a strictly given q_2 , one has to exclude the fission events occurred in the “previous” $q'_2 < q_2$ configurations, i.e.,

$$w'(q_3; q_2) = w(q_3; q_2) \frac{1 - \int_{q'_2 < q_2} w(q_3; q'_2) dq'_2}{\int w(q_3; q'_2) dq'_2}. \quad (16)$$

The normalized mass yield is then obtained as the integral of partial yields over q_2 :

$$Y(q_3) = \frac{\int w'(q_3; q_2) dq_2}{\int w'(q_3; q_2) dq_3 dq_2}. \quad (17)$$

Since there is a one-to-one correspondence between q_3 deformation and the masses of the left (A_L) and right ($A_R = A - A_L$) fission fragments, the yield given by Eq. (17) can be directly compared with the experimental FMY’s. Note that due to the normalization procedure (17), the scaling parameter k_0 introduced in Eq. (11) does no longer appear in the definition of mass yield.

So, there are only two free parameters in the above model, namely the zero-point energy E_0 in Eq. (9) and the half-width parameter d appearing in the probability of neck rupture in Eq. (12).

3 Fission fragment mass-yields

Relatively good estimates of the FMY’s obtained in our previous works [8, 9] for Pu and Pt to Ra isotopes encourage us to apply our model to describe and predict the mass yield for the low-energy fission of actinide nuclei from Th to Rf. Our main goal is to show that the innovatory Fourier shape parametrization [13] and the mac-mic model based on the LSD macroscopic energy [10] with the microscopic energy correction evaluated using the Yukawa-folded potential [11, 12] describes well the existing fission valleys in the broad region of nuclei. It is worth recalling that none of the model parameters, apart from E_0 and d described in the previous section, was modified here to get a better description.

In general, the theoretical estimates of FMY depend weakly on the choice of the free parameters E_0 and d . To obtain the best fit to the existing experimental FMY’s, the following overlap of theoretical and experimental yields:

$$I(E_0, d) = \sum_0^A \int |Y_{exp}(A_f) - Y_{th}(A_f; E_0, d)| dA_f. \quad (18)$$

is minimized with respect to E_0 and d . The sum in Eq. (18) runs over the nuclei, where the experimental data exist. Contrary to the ξ^2 fit, this fitting procedure does

not overestimate the role of large deviations. The optimised values $E_0 = 2.2$ MeV and $d = 1.6$ fm are finally used to obtain the FMY for all considered actinide nuclei.

It is well known that the FMY of a given nucleus is mainly determined by its PES properties at large deformations. Typical examples of PES for ^{240}Pu are shown in Fig. 2, where the mac-mic energy minimized with respect to q_4 is plotted on the (q_2, η) (top) and (q_2, q_3) (bottom) planes. The labels at the layers correspond to the energy of the deformed nucleus (in MeV) measured with respect to the LSD macroscopic energy of the spherical nucleus. The first saddle is visible around $q_2 = 0.55$ and $q_3 = 0$, while the second one is at $q_2 = 1.10$ and $q_3 = 0.08$. As one can see in the upper panel, the non-axial deformation η does not influence the PES at larger q_2 deformation. So, we do not take this degree of freedom into account in our analysis of the FMY’s. Let us notice that each of the 2D energy maps shown in Fig. 2 is only a projection of the full 4D PES, and one has to consider other cross-sections in order to analyze the fission process in details.

The fission fragment mass yields obtained in our model are presented in Figs. 5 to 8. Some experimental data for the FMY were obtained for the fission of excited nuclei. In such a case, we take this excitation into account and reduce the microscopic energy correction according to the prescription found in Ref. [27]. Our estimates of FMY correspond to the so-called pre-neutron yields, i.e., the mass yields before neutron emission from fragments and with such data (red stars in Figs. 5 to 8) they have to be compared. In the case of Th isotopes, we have used the fragment charge yields from Refs. [28, 29] and to obtain the mass-yields it is assumed that the Z/N ratio in the fragment is the same as in the mother nucleus. In cases when the pre-neutron data were not available, we have plotted the post-neutron data (blue crosses) just to get piece of information about the experimental situation. It is shown that for the Th isotopes, although the agreement of the estimates with the experimental data is not very satisfactory, the general trend is reproduced, i.e., a transition from symmetric to asymmetric fission is evidently reproduced with a growing mass number of isotope. The best agreement was achieved for ^{218}Th and $^{228-230}\text{Th}$ nuclei. The agreement with experimental data in the Uranium chain, presented in the bottom part of Fig. 5, is much better. Here the maxima and the widths of the fragment mass distribution are well reproduced, and a similar transition between symmetric and asymmetric fission as in Th isotopes is evident.

The prediction of the FMY’s for Pu and Cm isotopes are compared in Fig. 6 with the experimental data. The pre-neutron experimental yields for Pu [34] and ^{246}Cm [32] isotopes are obtained for the spontaneous fission case, while those for ^{244}Cm and ^{248}Cm are post-neutron yields taken from Ref. [3]. A nice agreement with the

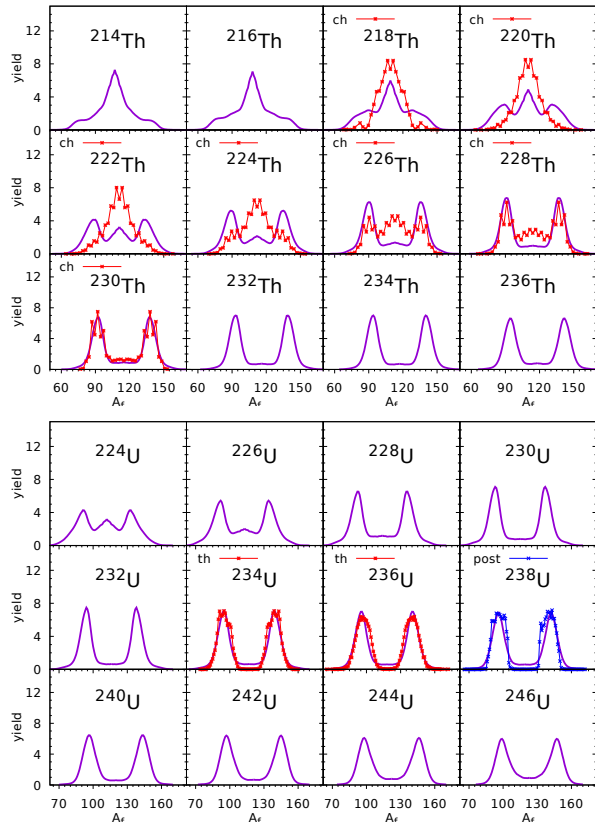


Fig. 5: Fission fragment mass-yields of Th (top part) and U (bottom part) isotopes. Experimental data (red stars) for Th isotopes are extracted from the charge-yields of Refs. [28, 29] while the mass-yields for U isotopes (bottom part) are taken from Ref. [30, 31] for the thermal neutron induced fission (th). Just to guide the eye we have used for ^{238}U the post-neutron data (blue crosses) taken from Ref. [3].

data obtained for the two lightest Pu isotopes ^{236}Pu and ^{238}Pu is slightly spoiled when the number of neutrons increases i.e. for ^{242}Pu and ^{244}Pu . It is mainly because we have used here the globally optimized values of E_0 and d , which are not fitted to Pu data only as done in Ref. [8]. In all investigated Pu and Cm isotopes here, the asymmetric fission is predicted with the mass of the heavy fragment $A \approx 140$.

The estimates of the FMY for Cf and Fm chains of isotopes are shown in Fig. 7. All experimental data correspond to the spontaneous fission, but only for ^{252}Cf [31] and ^{256}Cf [33] have to do with pre-neutron yields. The rest of the experimental yields presented in Fig. 7 corresponds to the post-neutron data (blue crosses). One can see that for lighter Cf and Fm isotopes, the asymmetric yields are predicted, while in the case of the heaviest Cf and Fm nuclei, the symmetric fission is foreseen. As one can deduce from the above results, our estimates are rather consistent with the experimental yields. A sim-

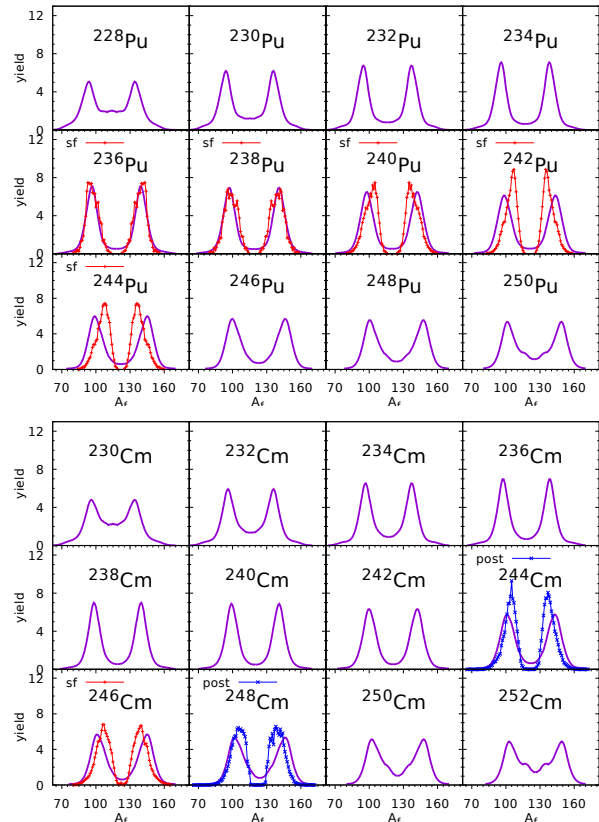


Fig. 6: Fission fragment mass yields of Pu (top part) and Cm (bottom part) isotopes. Experimental data (red stars) are taken from Ref. [34] for Pu chain and Refs. [3, 32] for Cm nuclei.

ilar tendency as seen in the Cf and Fm chains can be observed in Fig. 8 for the No and Rf isotopes, where the asymmetric fission is predicted in the lighter nuclei while the symmetric fission mode dominates for the isotopes with $N > 156$. The agreement with the experimental data of ^{256}No and ^{262}Rf [35, 37] is evident.

The overall good quality of our predictions in a broad mass region of the actinide elements is probably due to the fact that in very heavy nuclei, the fission barrier is very short, and the fission valley forms very early, i.e., at a relatively small elongation of the nucleus. An opposite situation occurs in the thorium nuclei, where the fission barriers are very broad. Fig. 9 presents the fission valley potential as a function of the elongation parameter q_2 . It is shown that the average slope of the curve from the last saddle to scission in the thorium nuclei is almost three times smaller than in nobelium. Obviously, such a large difference in the slope towards fission influences the fission dynamics in these both types of nuclei. This is a main reason why one has to study in details the PES in Th nuclei to explain here observed change in the FMY systematics.

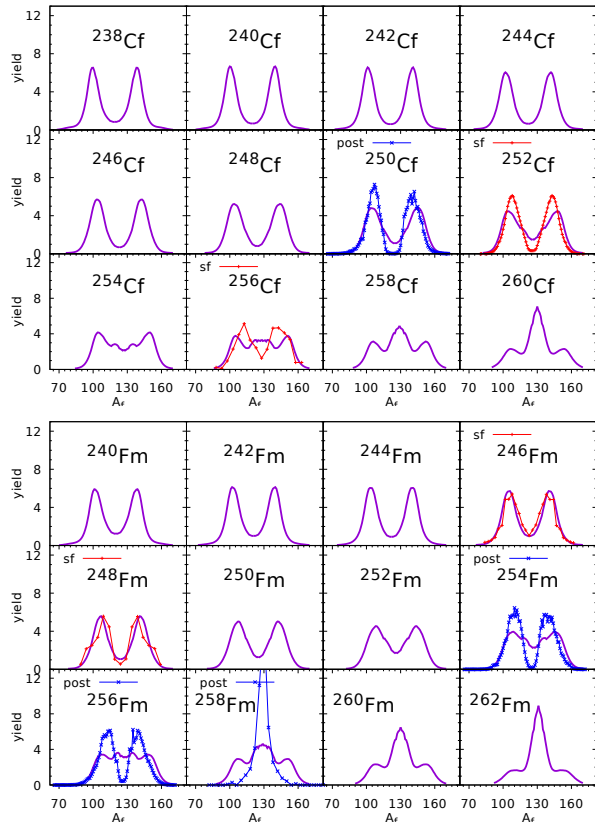


Fig. 7: Fission fragment mass yields of Cf (top) and Fm (bottom) isotopes. Experimental data for pre-neutron yields (red stars) are taken from Refs. [31, 33] while the post-neutron yields (blue crosses) origin from Ref. [3, 36].

4 Specific discussions on Th nuclei

The agreement of our estimates of the FMY's with the experimental data in the Th chain of isotopes depicted in Fig. 5 is not quantitatively satisfactory. So, in the present section, we would like to look for the origin of these discrepancies. First, these yields for the Th nuclei are evaluated using E_0 and d obtained by the fit to the data for all nuclei. The PES's for Th nuclei are very much different from those for heavier nuclei. This can be seen by comparing the PES of ^{240}Pu shown in Fig. 2 (bottom) with the corresponding maps for $^{218-230}\text{Th}$ isotopes presented in Fig. 10.

In ^{240}Pu , the fission path goes directly from the saddle point to the asymmetric fission valley in ^{240}Pu while it is not the case in ^{218}Th where the system from the 3rd minimum at $q_2 \approx 1.2$ has a much smaller barrier towards symmetric fission (< 0.5 MeV) than in asymmetric one, where the barrier is slightly higher (≈ 1 MeV) and thicker. It means that ^{218}Th nucleus prefers the sym-

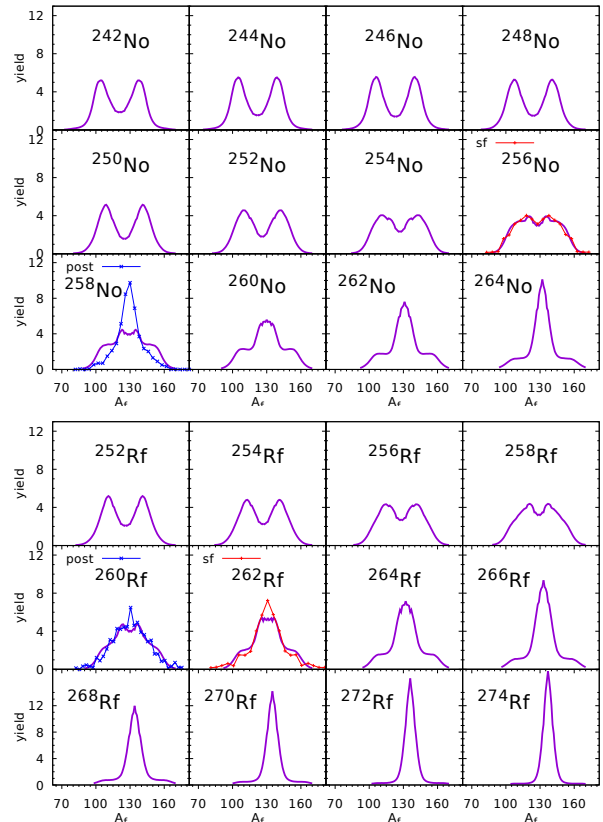


Fig. 8: Fission fragment mass yields of No (top) and Rf (bottom) isotopes. Experimental data (crosses) are taken from Refs. [35, 36, 37].

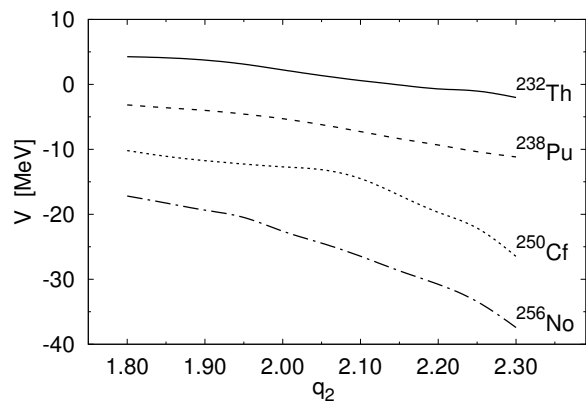


Fig. 9: Potential corresponding to the bottom of fission valley as a function of the elongation parameter q_2

metric fission, which is confirmed by the experimental yield. In ^{222}Th the situation is similar, while beyond ^{226}Th the path leading to the asymmetric fission begins to be preferred. To better understand this process, one has to study the PES's in the full 3D deformation space.

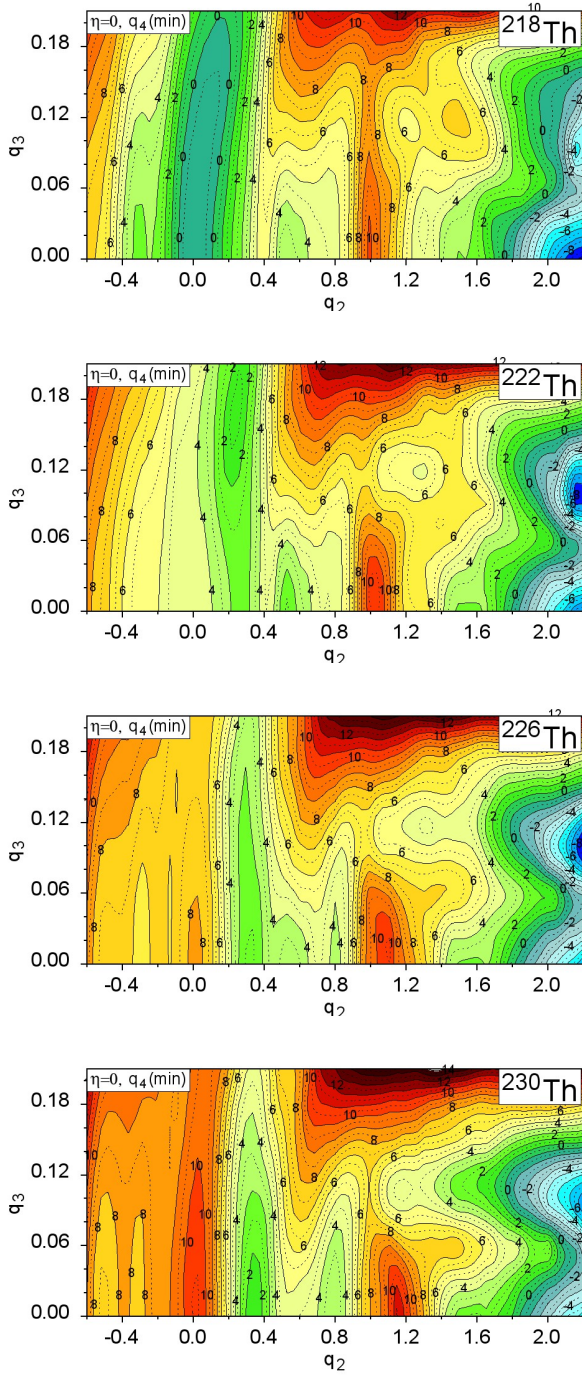


Fig. 10: Potential energy surface cross-sections of $^{218-230}\text{Th}$ isotopes minimized with respect the neck parameter q_4 on the plane (q_2, q_3) .

In Fig. 11 the (q_2, q_3) cross-sections of the PES for ^{218}Th corresponding to different elongations ($q_2 = 1.8, 2.0, 2.2,$ and 2.3) are shown.

Two minima, one corresponding to the symmetric

($q_3 = 0$) and the other to the asymmetric ($q_3 \approx 0.12$) configuration, are visible in each cross-section. At $q_2 = 1.8$

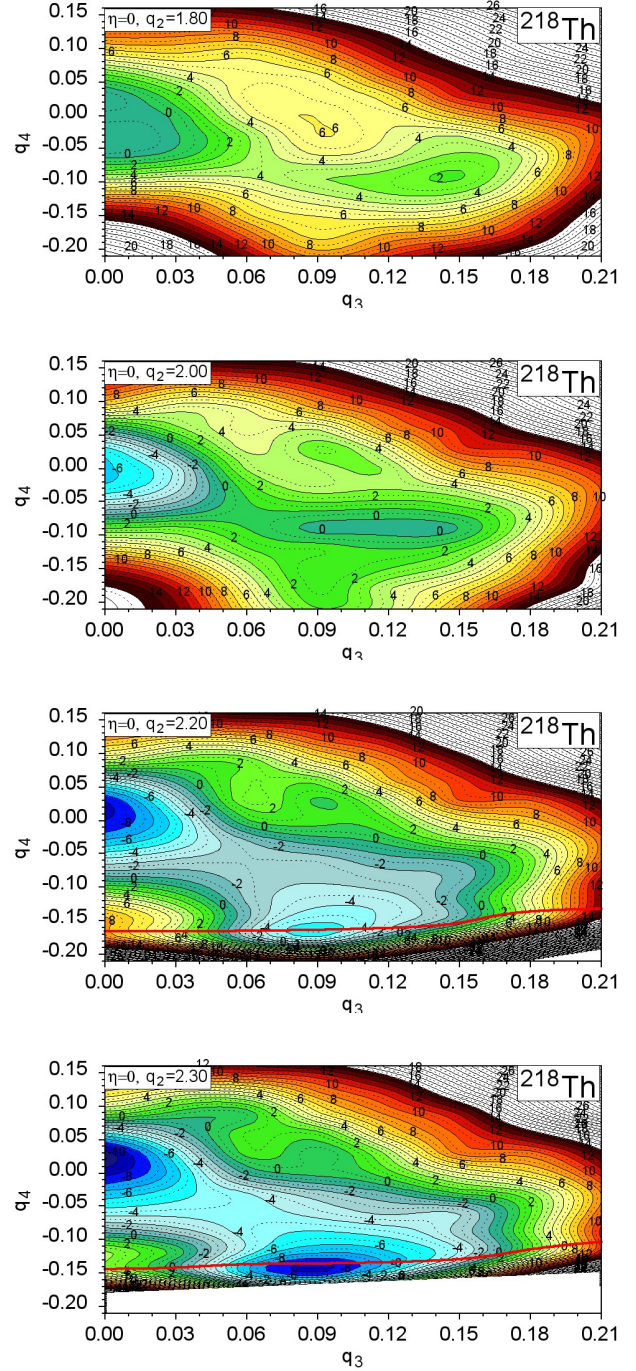


Fig. 11: Potential energy surface cross-sections of ^{218}Th on the plane (q_3, q_4) . The panels from top to bottom correspond to elongations $q_2 = 1.8$ to 2.3 , respectively. The solid red lines drawn in the bottom panels correspond to the neck radius equaling to the nuclear radius constant.

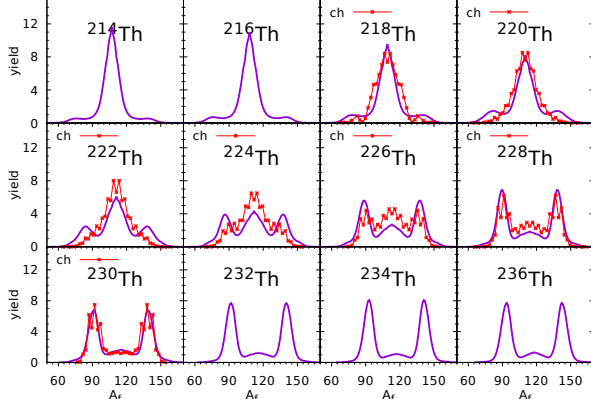


Fig. 12: Fission fragment mass yields of Th isotopes reproduced by using constants E_0 and d fitted to the experimental data (red stars) taken from Refs. [28, 29].

they are separated by a 4 MeV high barrier which becomes smaller with growing elongation q_2 , reaching finally 0.5 MeV height at $q_2 = 2.1$. At such elongations, the transition between the symmetric and asymmetric fission is possible. Both fission valleys are well separated again at the largest deformations close to the scission line (red line in the figure). So, the Th nuclei make the "decision" *where to go* pretty early, i.e., at an early stage far before the scission configuration. It means that one has to modify the adjustable parameters E_0 and d in order to better describe the transition between the symmetric and asymmetric fission modes observed in Th nuclei when the neutron number grows. The new fit performed to the data for Th isotopes only gives $E_0=1.5$ MeV and $d=2.5$ fm. The resulting mass yields are compared in Fig. 12 with the experimental data. This time the agreement is much more satisfactory. The new value of the neck parameter d is larger than that adjusted to all nuclei. It suggests that in Th nuclei, the choice of the preferable fission mode is made at a thicker neck, i.e., in a pretty early stage. The smaller value of E_0 used for Th isotopes is probably related to the competition between the symmetric and asymmetric minima.

5 Summary and conclusions

In order to briefly summarize our investigations, we can write:

- The overall accordance of the theoretical FMY estimates with the experimental data indicates that the mac-mic model with the LSD energy for the macroscopic smooth part and the shell and pairing corrections evaluated on the basis of the Yukawa-folded single-particle potential describes well the potential energy surfaces of actinide nuclei,

- Three-dimensional set of the Fourier deformation parameters used to describe the shape of fissioning nuclei are fully capable to produce a wide variety of the shapes of nuclei on their way to fission,
- The collective 3D model based on the Born-Oppenheimer approximation and comprising elongation, mass asymmetry, and neck modes reproduces well the main features of the fission fragment mass yields data,
- The Wigner function used to approximate the probability distribution related to the neck and mass asymmetry degrees of freedom simulates in a proper way this distribution for low-energy fission,
- A neck-breaking probability depending on the size of the neck has to be introduced to improve the accordance of our FMY estimates with the experimentally measured values.

Our mac-mic model and the collective 3D approach, which couples fission mode, neck, and mass asymmetry collective vibrations, can describe the main features of the fission process in actinide nuclei. The estimated fission barrier heights deviate not much from their experimental values. The measured fission fragment mass yields are also reproduced in a satisfactory way. On the other hand, one has to treat the presented collective model as a kind of rough tool which allows to obtain the FMY by a relatively quick calculation. To get more precise results, one has to use more advanced models in which the whole fission dynamics and the energy dissipation will be taken into account. Such calculations may use the Langevin dynamics (conf. Ref. [6]) or the improved quantum molecular dynamics model (ImQMD). The latter method has been successfully applied to describe the fission process in the heavy ion induced fission reactions, where the excitation energy increases, leading possibly to a shorter fission time scale and even to the occurrence of a ternary fission [38, 39].

The Langevin type calculations, profiting of the PES generated in a mac-mic approach together with the 3D Fourier shape parametrization as well with the use of the self-consistent method, are carried out in parallel by our group.

Acknowledgments

The authors would like to thank Christelle Schmitt and Karl-Heinz Schmidt for supplying us with a part of the experimental data.

References

- [1] M. R. Mumpower, P. Jaffke, M. Verriere, J. Randrup, Phys. Rev. C **101**, 054607 (2020).

- [2] J. Randrup, P. Möller, Phys. Rev. C **88**, 064606 (2013).
- [3] K.-H.Schmidt, B.Jurado, C.Amouroux, C.Schmitt, Nucl.Data Sheets **131**, 107 (2016).
- [4] A. Baran, M. Kowal, P.-G. Reinhard, L.M. Robledo, A. Staszczak, M. Warda, Nucl. Phys. A **944**, 442 (2015).
- [5] P. Jachimowicz, M. Kowal, J. Skalski, Phys. Rev. C **101**, 014311 (2020).
- [6] H. J. Krappe, K. Pomorski, *Theory of Nuclear Fission*, Lecture Notes in Physics 838, Springer-Verlag, 2012, DOI 10.1007/978-3-642-23515-3.
- [7] K. Pomorski, F. A. Ivanyuk, B. Nerlo-Pomorska, Eur. Phys. Journ. **A53**, 59 (2017).
- [8] K. Pomorski, B. Nerlo-Pomorska, J. Bartel, C. Schmitt, Eur. Phys. Journ. Web Conf. **169**, 00016 (2018).
- [9] K. Pomorski, A. Dobrowolski, R. Han, B. Nerlo-Pomorska, M. Warda, Z.G. Xiao, Y.J. Chen, L.L. Liu, J.L. Tian, Phys. Rev. C **101**, 064602 (2020).
- [10] K. Pomorski, J. Dudek, Phys. Rev. C **67**, 044316 (2003).
- [11] K. T. R. Davies and J. R. Nix, Phys. Rev. C **14**, 1977 (1976).
- [12] A. Dobrowolski, K. Pomorski, J. Bartel, Comp. Phys. Comm. **199**, 118 (2016).
- [13] K. Pomorski, B. Nerlo-Pomorska, J. Bartel, and C. Schmitt Acta Phys. Pol. B Supl. **8**, 667 (2015).
- [14] C. Schmitt, K. Pomorski, B. Nerlo-Pomorska, J. Bartel, Phys. Rev. C **95**, 034612 (2017).
- [15] J. Bartel, K. Pomorski, B. Nerlo-Pomorska, H. Molique, Acta Phys. Pol. B Supl. (2020) in print.
- [16] V. M. Strutinsky, Sov. J. Nucl. Phys. **3**, 449 (1966); Nucl. Phys. A **95**, 420 (1967); Nucl. Phys. A **122**, 1 (1968).
- [17] S.G. Nilsson, C. F. Tsang, A. Sobiczewski, Z. Szymański, S. Wycech, S. Gustafson, I. L. Lamm, P. Möller, B. Nilsson Nucl. Phys. A **131**, 1 (1969).
- [18] K. Pomorski, Phys. Rev. C **70**, 044306 (2004).
- [19] J. Bardeen, L. N. Cooper, J. R. Schrieffer, Phys. Rev. **108**, 1175 (1957).
- [20] A. Gózdź, K. Pomorski, Nucl. Phys. A **451**, 1 (1986).
- [21] S. Pilat, K. Pomorski, A. Staszczak, Zeit. Phys. **A332**, 259 (1989).
- [22] G. N. Smirenkin, IAEA-Report INDC(CCP)-359, (1993).
- [23] W. D. Myers, W. J. Świątecki, Nucl. Phys. A **601**, 141 (1996).
- [24] A. Dobrowolski, B. Nerlo-Pomorska, K. Pomorski, Acta Phys. Polon. B **40**, 705 (2009).
- [25] E. Werner, H.S. Wio, H. Hofmann, K. Pomorski, Z. Phys. A **299**, 231 (1981).
- [26] J. Randrup, S. E. Larsson, P. Möller, S. G. Nilsson, K. Pomorski, A. Sobiczewski, Phys. Rev. C **13**, 229 (1976).
- [27] B. Nerlo-Pomorska, K. Pomorski, J. Bartel, Phys. Rev. C **74**, 034327 (2006).
- [28] K.-H. Schmidt et al., Nucl. Phys. **A665**, 221 (2000);
- [29] A. Chatillon et al. Phys. Rev C **99**, 054628 (2019).
- [30] P. Geltenbort et al., Conf. on Nucl. Data Basic Appl. Sci., Santa Fe 1985, Vol.1, p.393 (1985), USA.
- [31] C. Romano et al. Phys. Rev. C **81**, 014607 (2010).
- [32] F.Pleasanton et al., Phys. Rev. C **8**,1018 (1973).
- [33] D. C. Hoffman et al., Phys. Rev. C **21**, 972 (1980).
- [34] L. Dematté, C. Wagemans, R. Barthélémy, P. D'hondt, A. Deruytter, Nucl. Phys. **A617**, 331 (1997).
- [35] D. C. Hoffman et al. Phys. Rev. C **41**, 631 (1990).
- [36] E. K. Hulet et al., Phys. Rev. Lett. **56**, 313 (1986).
- [37] M. R. Lane et al., Phys. Rev. C **53**, 2893 (1996).
- [38] Q. H. Wu, X. Y. Diao, F. H. Guan, Y. J. Wang, Y. X. Zhang, Z. X. Li, X. Z. Wu, K. Pomorski, and Z. G. Xiao, Phys. Lett. B **797**, 134808 (2019).
- [39] Q. H. Wu, F. H. Guan, X. Y. Diao, Y. J. Wang, Y. X. Zhang, Z. X. Li, X. Z. Wu, A. Dobrowolski, K. Pomorski, Phys. Lett. B **811**, 135865 (2020).